MDPI

Article

Proper Orthogonal Decomposition Based Response Analysis of Inlet Distortion on a Waterjet Pump

Puyu Cao [1], Rui Yue [1], Jinfeng Zhang [1,*], Xinrui Liu [2], Gang Wu [3] and Rui Zhu [1]

[1] Research Center of Fluid Machinery Engineering and Technology, Jiangsu University, 301 Xuefu Road, Zhenjiang 212013, China; mafatu1988@ujs.edu.cn (P.C.); yurie200805793@163.com (R.Y.); ruizhu@stu.xjtu.edu.cn (R.Z.)

[2] Wenling Fluid Machinery Technology Institute, Jiangsu University, Wenling 317525, China; liuxinrui5152022@163.com

[3] Zhejiang Doyin Technology Co., Ltd., No. 19, South of Songhang Road, Eastern New District, Wenling 318000, China; 8971136@99.com

* Correspondence: zhangjinfeng@ujs.edu.cn; Tel.: +86-137-7647-6981

Abstract: This study addresses the challenge of performance degradation in waterjet pumps due to non-uniform suction flow. Utilizing the Proper Orthogonal Decomposition (POD) method, it decomposes and reconstructs the flow features within a waterjet pump under non-uniform inflow into a series of modes ranked in descending order of energy. By analyzing the modes with dominant energy, which contain complex information about the flow field, it is revealed that modes 1 and 2 predominantly represent the formation of a concentrated vortex, whereas modes 3 and 4 illustrate its spatial offset. Notably, in the hub section, mode 3 exhibits a delayed flow separation caused by the reduction of circumferential vortex (CV), with a consequent lift in blade loading at the leading edge and a higher head compared to mode 1. In the shroud section, the delayed flow separation in mode 3 suppressed reverse flow and the concentrated separation vortex (CSV) and then increased the blade loading, ultimately enhancing the pump head. The findings provide significant insights into optimizing waterjet pump performance by detailing the interactions between various flow structures and pump components, effectively filling a knowledge gap in applying dimensionality reduction techniques within the distorted flow fields of water jet pumps.

Keywords: proper orthogonal decomposition; water jet pump; vortex; blade loading

1. Introduction

Waterjet propulsion is a unique method of marine propulsion that distinctly differs from traditional propeller propulsion, its sketch is shown in Figure 1. Unlike traditional propellers, waterjet propulsion does not generate thrust directly; rather, it employs a waterjet pump to expel water flow, thereby propelling the vessel forward through reactive force. This innovative propulsion system offers several advantages over traditional propellers, including increased maneuverability, reduced draft, and the ability to operate in shallow water [1,2]. This propulsion technique offers numerous advantages, including high efficiency, robust cavitation resistance, smooth operation, low noise levels, minimal risk of overload, and reduced hull resistance. Consequently, waterjet pumps find extensive application in high-speed vessels and silent submarines [3,4]. However, a long-standing challenge has been the significant hydraulic losses and low efficiency of the pipeline system due to distorted inflow in the intake channel [5]. The structural limitations of the intake channel and disturbances caused by driving shafts result in non-uniform circumferential inflow velocities during waterjet pump operation, with lower velocities observed on the upper wall surface compared to the lower wall surface. The varying curvature radii between these surfaces create different inertial forces during flow bending that disrupt

pressure-inertial force equilibrium and induce lateral pressure differences. As a consequence, secondary flows superimpose on primary flows, leading to complex helical flow patterns similar to those observed in curved pipe inflows. Simultaneously, at low speed under lateral pressure differences induced by this flow pattern, fluid enters a low-energy zone (with reduced velocity and relatively low pressure) within the middle section of the upper wall surface, causing uneven working fluid to enter the impellers.
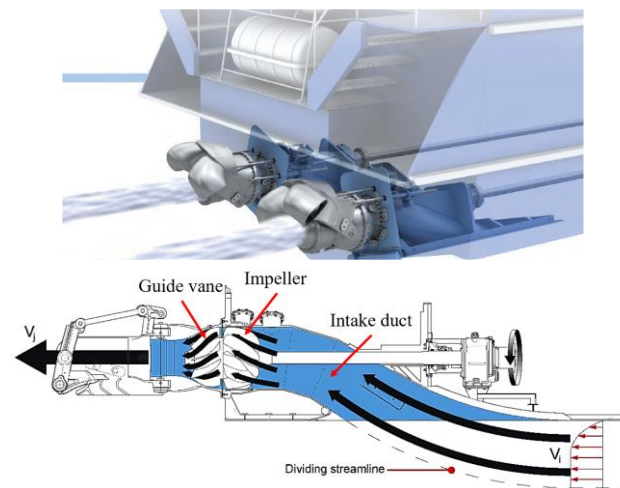
Figure 1. Sketch of a waterjet pump.

Numerous studies have documented the presence of uneven suction flows within the entire waterjet propulsion mechanism, striving to pinpoint the origins and configurations of these non-uniform flows through experimental or computational approaches. Duerr [6] qualitatively described the process and reasons for the decline in lift of waterjet pumps under inflow distortion from the perspective of waterjet pump design. Bulten [7] used simulation methods to calculate the efficiency of waterjet propulsion pumps under uniform and distorted inflows, finding that the efficiency of waterjet propulsion pumps indeed decreases under inflow distortion, but the reduction is limited. Van Esch [8] explored the impact of asymmetric inlet structures on waterjet propulsion pumps from an experimental standpoint. The results indicated that the inflow distortion generated in front of the pump led to reductions in the mixed-flow pump's torque, lift, and axial force, with the lift decreasing by approximately 2.5%.

With advancements in computational fluid dynamics and sophisticated flow measurement techniques, the depiction of flows has become increasingly detailed. Consequently, the extraction of flow field modes and the modeling of complex dynamical characteristics have emerged as focal points of current research in fluid mechanics [9,10].However, due to the computational complexity and challenges in data acquisition, experts in fluid mechanics often develop simplified models based on the original flow field and employ data reduction techniques to extract essential features [11–16].

Utilizing the Proper Orthogonal Decomposition approach, Wang J. et al. [17] investigated the dynamics of flow around dual two-dimensional cylinders placed parallel to each other at varying distances. Their findings reveal that with a separation of g = 1.5 m, the interaction between the cylinders is minimal, creating a wake with periodic, synchronized patterns in the same direction. Conversely, a tighter separation of g = 0.35 m results in heightened interference, complicating the flow and producing an alternating wake pattern where the flow's periodicity becomes less defined. Song et al. [18]. leveraged POD techniques for data reduction, streamlining the number of design variables in optimization processes. Chen [19] integrated POD and DMD to dissect the intricate flow within centrifugal pumps, devising an adaptive POD model based on clustering for efficient blade redesign and pump performance enhancement. Ye [20] utilized the mode decomposition method to study the unsteady flow field around the NACA0009 hydrofoil with a blunt

trailing edge and found that the DMD method can accurately extract the mode flow field structure, and the obtained mode frequency is unique. Tang [21] used the POD method to study the time-frequency characteristics and influencing factors of unsteady aerodynamic forces of airfoil under feathering conditions and found that the pressure distribution of the main-order modes of airfoil with tower presents a symmetrical form, and aerodynamic fluctuations mainly come from symmetrical pressure fluctuations of airfoil, resulting in aerodynamic mean deviation and fluctuation.

The POD method is widely applied in research fields such as flight dynamics [22], fluid–structure interaction [23], and flow control [24]. However, in the area of the internal flow characteristics of waterjet pumps, research related to this method is still scarce.

This study employs the Proper Orthogonal Decomposition (POD) method, a powerful approach for reducing the complexity of flow fields, to decompose the distorted flow field in waterjet propulsion pumps into distinct mode components. The primary objectives of this research are to systematically extract and analyze the dominant modes to uncover deeper physical phenomena that significantly impact pump performance. Specifically, the study aims to:

(1) Identify and characterize the most influential modes within the pump's flow field, focusing on their spatial distribution and energy levels.
(2) Investigate the dynamic interactions between these modes and the pump's structural components to understand their collective influence on pump performance.
(3) Utilize these insights to propose modifications that could potentially enhance the design and functionality of waterjet pumps, thereby increasing their performance.

2. Materials and Methods

Proper Orthogonal Decomposition (POD) is a mathematical technique employed for reducing data dimensionality and extracting primary features. It is a statistical and linear algebra-based method commonly utilized in fields such as fluid mechanics, structural dynamics, and signal processing. In POD, a set of data samples taken in time or space are considered, which can include flow field data, structural response data, or other signal data. The objective of POD is to identify the dominant features or vibration modes within this dataset and rank them in descending order of significance.

The main ideas behind the POD method are shown as follows:

At any given moment, the flow field x_i (such as velocity and pressure) can be represented as a superposition of the mean flow $\overline{x_i}$ and the fluctuating component x_i'.

$$x_i = \overline{x_i} + x_i' \tag{1}$$

The essence of utilizing Proper Orthogonal Decomposition (POD) for flow field representation lies in expressing the fluctuating momentum by means of a linear combination of low-order POD bases, namely:

$$x_i' = \sum_{j=1}^{N} a_j(i) \boldsymbol{u}_j(x) \tag{2}$$

Among them, N represents the number of snapshots in the flow field, $\boldsymbol{u}_j(x)$ denotes the POD basis, and $a_j(i)$ represents the mode coefficients of the i-th POD basis at time i. To obtain the POD basis, it is necessary to first acquire the fluctuating flow field P.

$$P = \left[x_1', x_2', x_3', \dots x_n' \right] \tag{3}$$

P is a matrix composed of the spatially sequenced, fluctuating momentum of the flow field velocity. Perform Singular Value Decomposition (SVD) on matrix P to obtain the left singular matrix U, eigenvalue matrix σ, and right singular matrix V^T.

$$P = U * \sigma * V^T \tag{4}$$

The matrix $U = [u_1, u_2, u_3, \ldots u_n]$ represents a collection of column modes, where σ is a diagonal matrix formed by arranging the eigenvalues of matrix P in descending order, and $V^T = [v_1, v_2, v_3, \ldots v_n]^T$ denotes a matrix consisting of row modes, typically expressed in transposed form. The POD basis can be obtained from the following equation:

$$\boldsymbol{u}_j(x) = u_j * v_j^T \tag{5}$$

The corresponding mode coefficient is:

$$a_j(i) = \sigma_i \tag{6}$$

where $a_j(i)$ represents the energy amount of every single mode.

3. Geometry and Mesh Setup

In recent years, numerous studies have provided evidence that numerical simulations can effectively forecast the performance of waterjet pumps and the entire waterjet propulsion system [25–27]. Hence, this paper utilizes the commercial software ANSYS-CFX 2022R1 to conduct steady calculations. The computational domain of the waterjet propulsion pump under non-uniform inflow is partitioned into five distinct regions, namely the nozzle, stator, rotor, intake duct, and control body of the flow field, as illustrated in Figures 2 and 3.
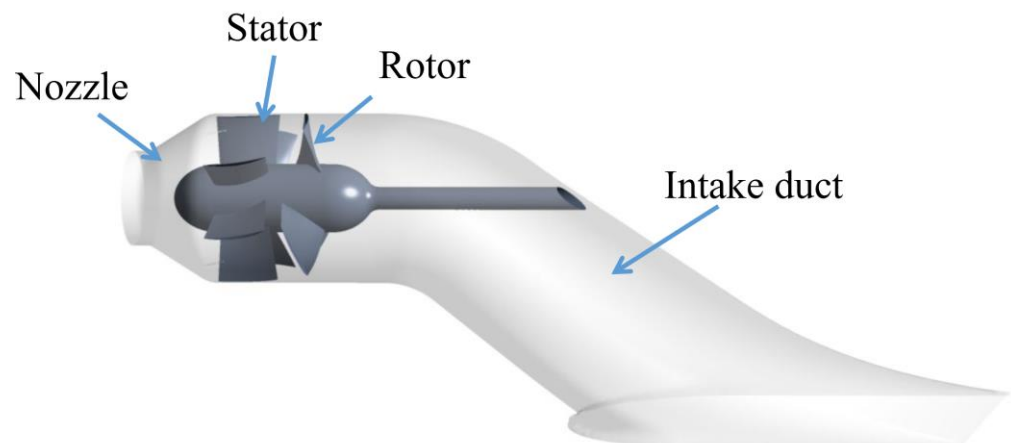
Figure 2. Geometry of the waterjet pump.
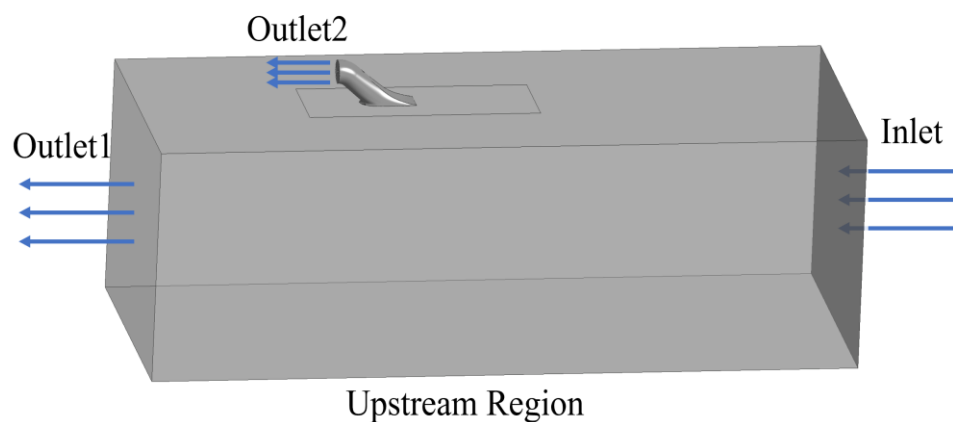
Figure 3. Geometry of the control body.

For numerical simulation, the ICEM 2022R1 grid software was employed to generate hexahedral grids for the intake duct, rotor, stator, and nozzle as depicted in Figure 4. The

rotor and stator were discretized using H-shaped blocks, while O-type partitioning was applied to the nozzle. Specifically, the wall grids of the rotor and stator were refined to ensure compliance with y+ requirements in near-wall regions during numerical calculations. Four different grid schemes were proposed while maintaining the block distribution form. Based on these four grid schemes, numerical solutions for the head value of a waterjet propulsion pump under design conditions were obtained. After conducting a grid independence test, it was determined that both the head difference and radial velocity variation between scheme 3 and scheme 4 were less than 1%. Therefore, scheme 3 was selected to complete the computational domain for a waterjet propulsion pump under uniform inflow conditions. The total number of grids in this scheme is approximately three million, with all grid qualities exceeding 0.5, as shown in Figure 5, and the average y+ is around 40, which is suitable for the RNG k-ε model. The accuracy of the RNG k-ε model has been validated by Chang [28].

(a)   (b)

(c)
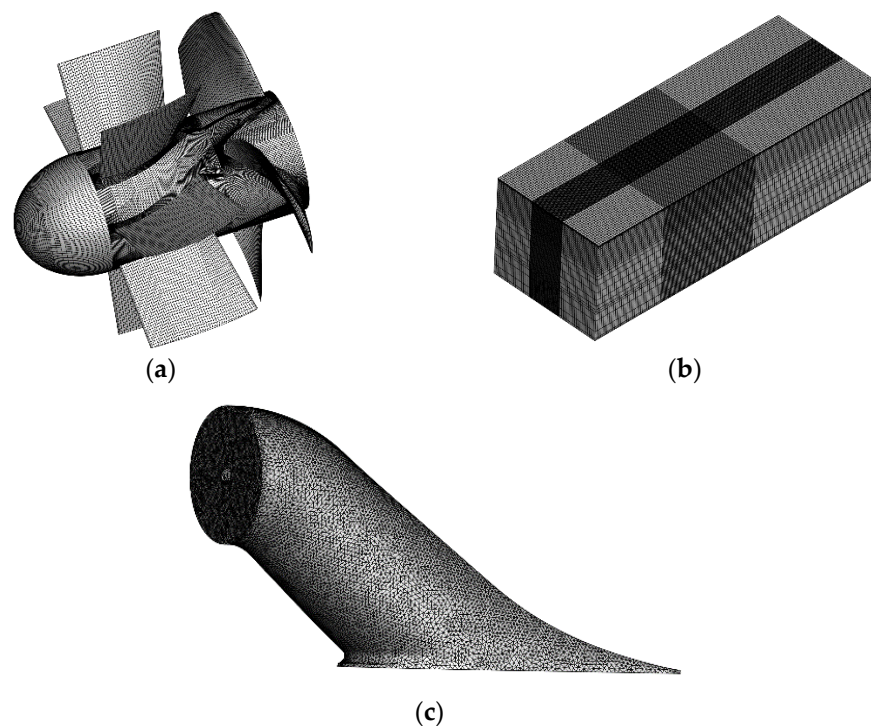
Figure 4. 3D multi-block grid in the waterjet propulsion pump: (**a**) rotor and stator mesh; (**b**) upstream region mesh; (**c**) intake duct mesh.

In the vessel's reference frame, the intake duct was designated as a non-moving frame, while the drive shaft was configured to rotate relatively at a speed of 1450 rpm. The upstream region was also set as a stationary frame, but the side and lower walls of the domain below the hull were set as relative motion (30 knots). The impeller domain was set as the rotating frame with a design shaft speed of 1450 r/min, where the hub and blades were set as relatively stationary while the casing was absolutely stationary. The stator and nozzle were also set as a stationary frame, where body surfaces were set as absolutely stationary. At the upstream region's outlet, an average static pressure was set as a boundary condition, and the nozzle's outlet was designated as an opening. During the calculation, the high-resolution scheme was used for the convection terms, while the central difference scheme was used for the diffusion terms. The convergence precision was based on reducing the maximum of the normalized residuals of the momentum and continuity equations to less than 10^{-5}. The fluid was ideal water at 25 °C. The inlet boundary condition was defined by a velocity normal to the entry point, with the initial velocity profile established by Equation (7). This actual velocity at the inlet accounted for

the ship's speed and included a consideration of the velocity gradient due to the boundary layer beneath the hull, calculated using the Wieghardt equation [29].

$$\text{Inlet velocity :} \qquad v_{in} = \begin{cases} v_s \left(\frac{y}{\delta} \right)^{1/N}, y \leq \delta \\ v_s, y \geq \delta \end{cases} \tag{7}$$

$$\text{Boundary layer thickness :} \quad \delta = 0.27 x_W (Re)^{-1/6} \tag{8}$$

where v_s is the ship speed, y is the depth normal to the hull bottom, the power law exponent $N = 9$ is used, and Re is the Reynolds number in relation to the wetted length x_W.
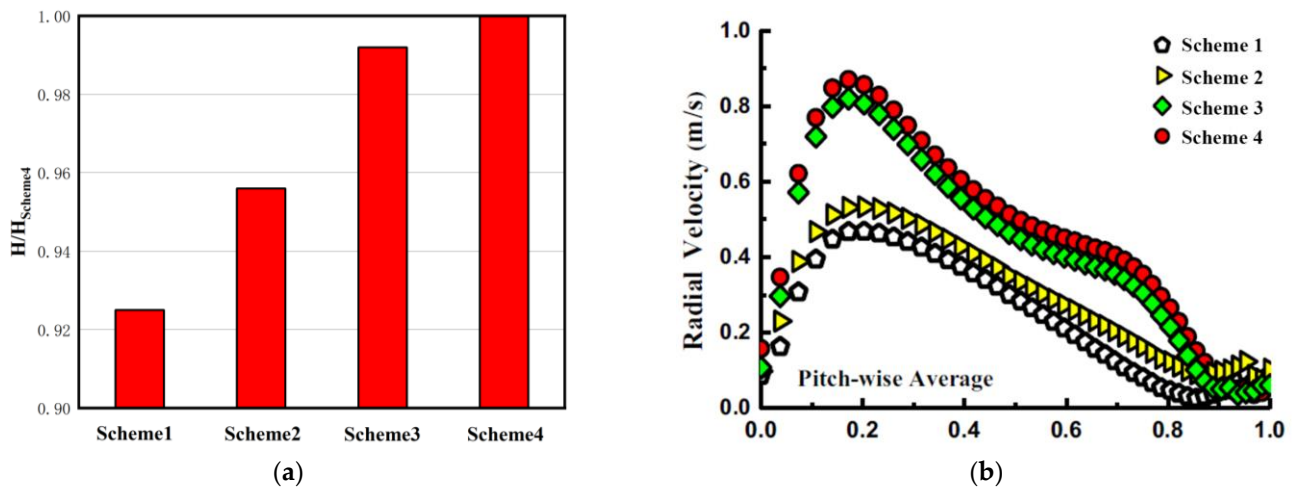
Figure 5. Grid independence analysis—(**a**) normalized pump head at design point; (**b**) design point: The radial velocity at the leading edge of the impeller blade is distributed spanwise, with an average taken over multiple pitches.

4. Mode Decomposition of the Distortion Field

The velocity field of the distortion flow will be sampled at intervals of 1°, with each sampling comprising 20 data points to construct a matrix P containing a total of 7200 data points. Subsequently, matrix P will undergo Proper Orthogonal Decomposition (POD) analysis, yielding distribution maps for the initial 20 modes and their corresponding energy percentages as depicted in Figure 6a. The accumulated energy of the first four modes (Figure 6b) accounts for 97%, indicating that the original in-flow field can be accurately represented solely by these modes.

Figure 7 is the 2D velocity contour of the inflow distorted field after POD decomposition. The comparison between the original inflow distorted field and the velocity contour of different modes reveals that the first-order mode exhibits the highest similarity with the original inflow distorted field. In mode 1 (b), a prominent concentrated vortex within the inflow distorted field is clearly observed. The edges of the low-speed region are well defined, and its extent remains relatively unchanged compared to the original flow field. However, a notable upward and rightward shift in the position of the concentrated vortex is observed when compared to the original inflow field.

(**a**)

(**b**)
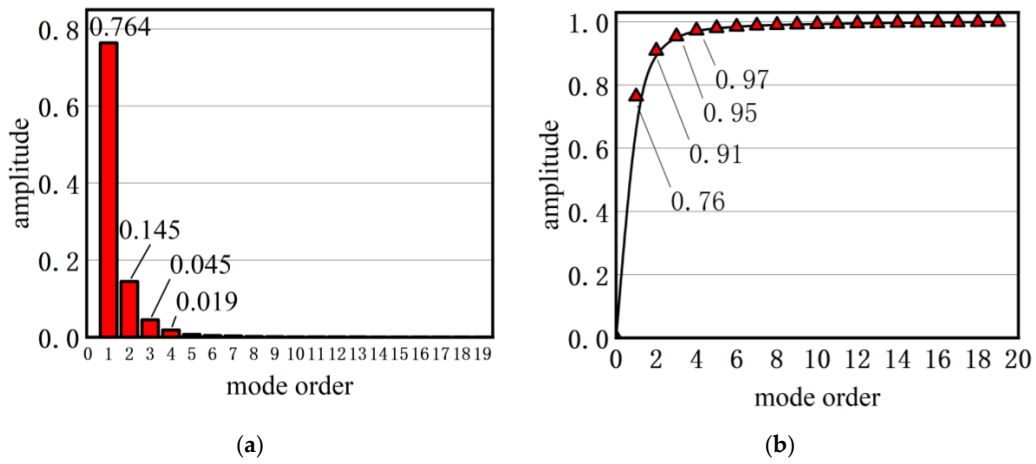
Figure 6. (**a**) Energy distribution of mode 1 to mode 20 (**b**) Energy accumulation from mode 1 to mode 20.

(**a**)

(**b**)

(**c**)

(**d**)

(**e**)
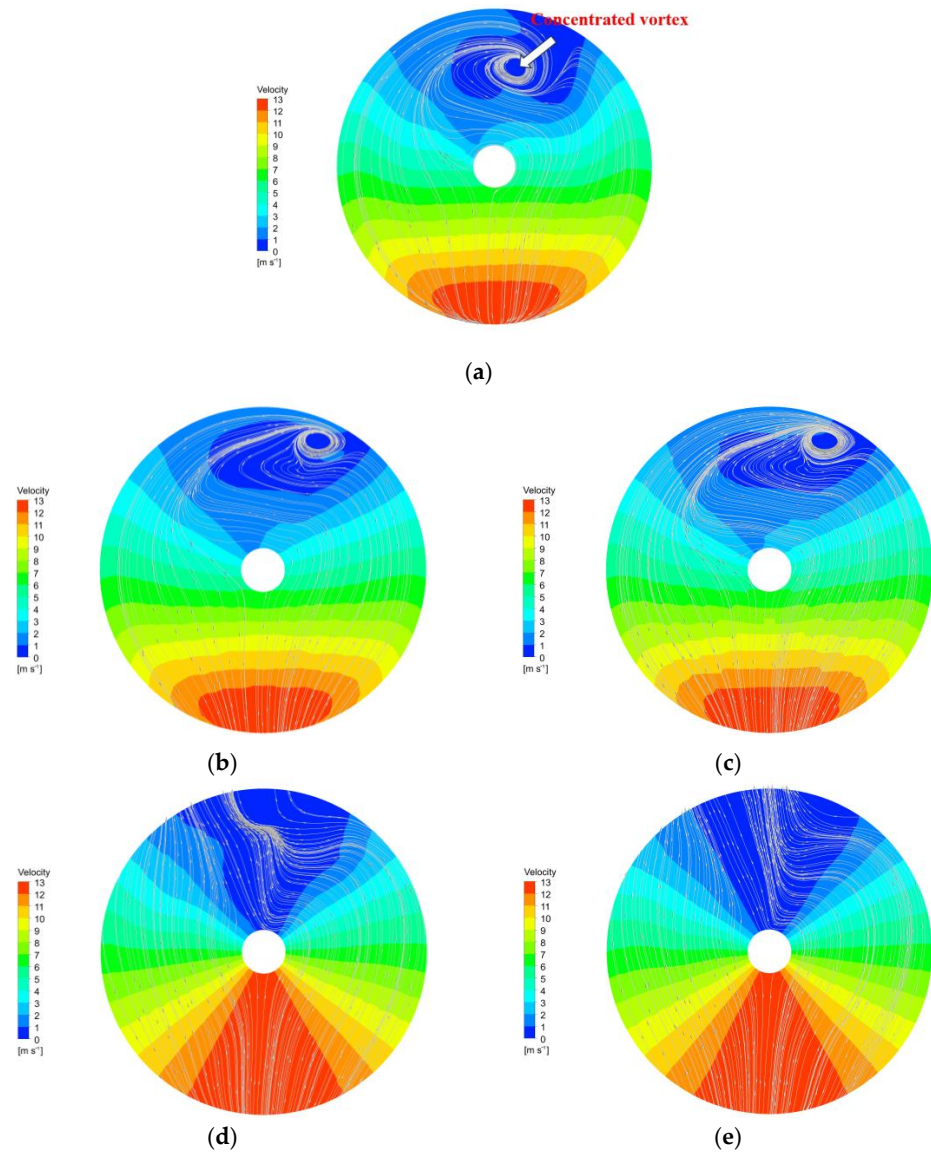
Figure 7. The 2D velocity contour of the inflow distortion field after POD decomposition: (**a**) original inflow field; (**b**) inflow field of mode 1; (**c**) inflow field of mode 2; (**d**) inflow field of mode 3; (**e**) inflow field of mode 4.

Moving on to mode 2 (c), similar characteristics of the concentration vortex are exhibited, albeit with a significant reduction in the size of the low-speed region. Furthermore, the edges of the various velocity layers present a jagged and complex morphology. In contrast, mode 3 (d) and 4 (e) no longer reveal the presence of a concentrated vortex, and the flow fields gradually converge towards an average flow field. Despite its absence, a pronounced spanwise deflection of the velocity streamlines remains evident. This deflection is primarily driven by the deflection of the 3rd and 4th-order velocities, ultimately influencing the repositioning of the concentrated vortex in modes 1 and 2 towards its original location.

In summary, mode 1 and 2 primarily characterize the formation process of the concentration vortex, while mode 3 and 4 determine its offset characteristics. This finding provides crucial insights for a deeper understanding of vortex structures and their dynamic evolution within fluid flow fields.

5. Results and Discussion

According to previous research [29–31], non-uniform inflow conditions of waterjet pumps exhibit four distinct vortex structures: concentrated separation vortex (CSV), circumferential vortex (CV), hub spanwise vortex (HSV), and flow separation. To investigate the relationship between these vortex structures and pump performance, four modalities were utilized as boundary conditions in the subsequent CFD calculation for further study of flow field analysis. The results are presented below.

Figure 8 illustrates variations in head measurements obtained from different mode responses in comparison with the original inflow condition. It is apparent that both first and second mode responses closely approximate those observed within the original flow field, whereas notable improvement in head performance can be seen with regard to the third and fourth mode responses, exhibiting an increase of 6.14%. The underlying factors that contribute to the augmentation of pump heads remain enigmatic. To gain a fundamental understanding of this phenomenon, the present study delves into the intricacies of the waterjet pump's impeller, specifically examining the blade loading distribution, blade static pressure, and vortex structure distribution at the shroud and hub.
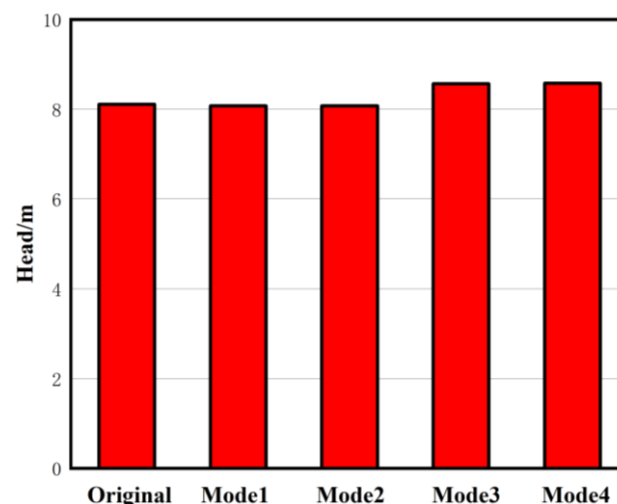
Figure 8. The pump head originated from multiple mode responses calculated by CFD.

5.1. Blade Loading

The nature of the concentrated vortex on the pump inlet surface is essentially a streamwise vortex, which interacts with the rotating impeller while flowing downstream. This inflow distortion further evolves into a circumferential vortex (CV, Figure 9a). Based on the CV, the impeller inlet surface is decomposed into a blockage zone and a flow-through zone, as shown in the side view of Figure 9b. Therefore, this paper analyzes the difference

in head between the first-order and third-order modes in Figure 8 from the perspective of blade loading in the hub and shroud regions.

(a)

(b)
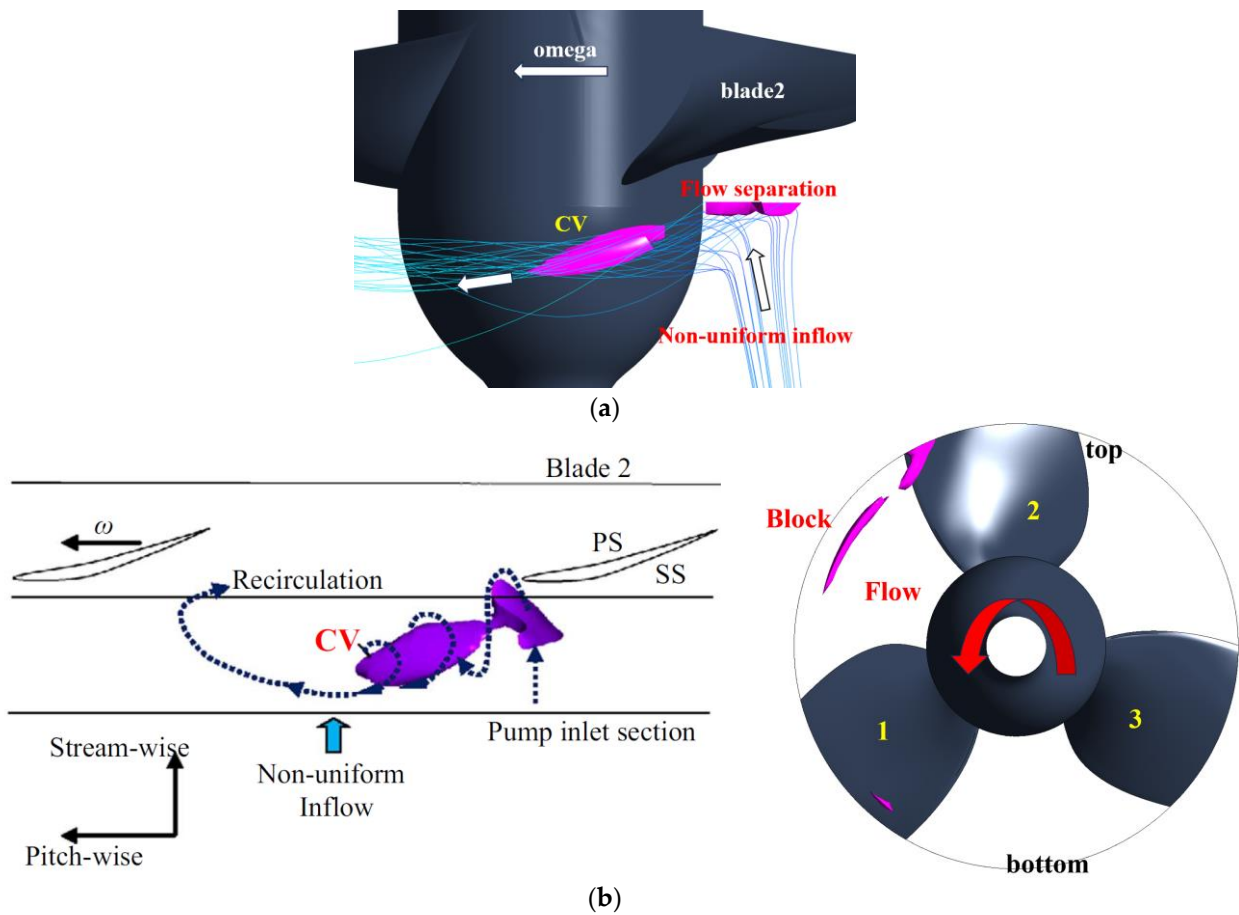
Figure 9. (**a**) Non-uniform suction flow evolves into a circumferential vortex (CV). (**b**) Side view of the rotor, and the blades are marked with numbers.

Bonaiuti [32,33] introduced the blade loading coefficient (C_L) as a metric to characterize the work-performing capability of blades. To simplify subsequent analysis and capitalize on the conjugate nature of modes, only the first and third modes were considered for investigation. Figure 9b illustrates the numbering scheme for blade positions. It is important to note that "blade 2" does not refer to a specific blade among the three in the impeller but rather represents all blades passing through the low-total-pressure region at the top. Based on the simulated results of the first and third modes of the waterjet pump at the design speed, the blade load coefficients (C_L) were calculated for each blade and plotted in Figure 10. This approach provides a more rigorous and specialized representation of the blade's performance characteristics.

Euler's equation:

$$gH_{\mathrm{t}} = \frac{\omega}{2\pi}(\Gamma_2 - \Gamma_1) \tag{9}$$

$$\Gamma = 2\pi v_u r \tag{10}$$

where: H_{t} is the theoretical head, m; ω is the angular velocity of rotation, rad/s; Γ is the velocity circulation, m^2/s; v_u is the component of the absolute velocity in the circumferential direction, m/s.

Normalized blade loading:

$$C_L = \frac{\partial(v_u r)}{\partial m} \bullet \frac{1}{\omega r_3^2} \tag{11}$$

where m is the dimensionless meridional distance, 0 is the inlet, and 1 is the outlet. ω is the angular speed, and r_3 is the impeller radius.
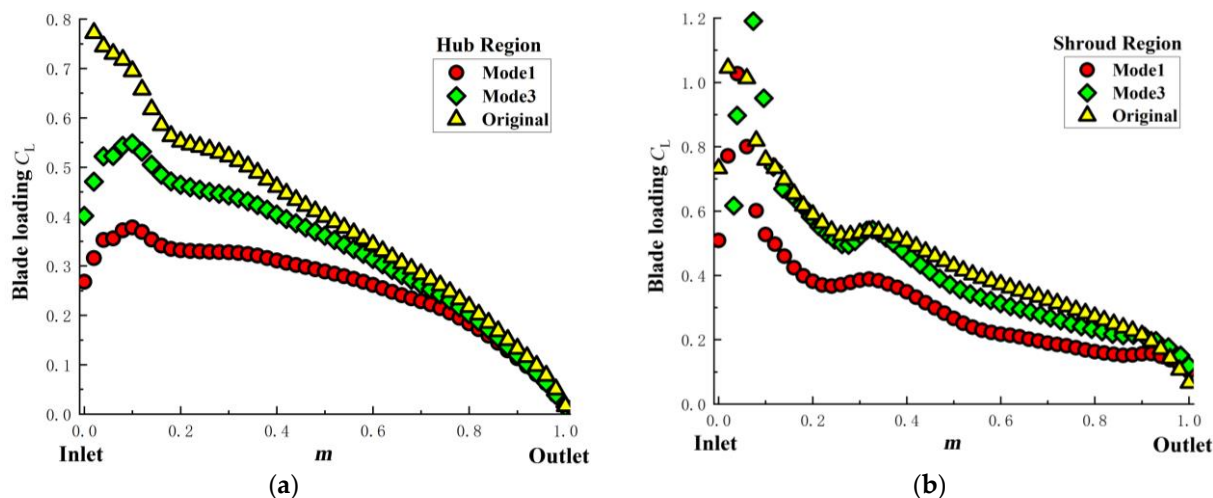
Figure 10. Normalized blade loading distributions of blade 2 in (**a**) the hub section; (**b**) the shroud section; among mode 1, mode 3, and the original.

The integral value of the blade loading distribution coefficient, which represents the enclosed area of the loading curve, is related to the blade circulation and characterizes the blade's work-performing capability according to Equation (9).

Figure 10a is a comparative graph of the load coefficients at the hub for blade 2 among the original flow field, mode 1 and mode 3. From the figure, it can be observed that, compared to the original inflow, mode 1 exhibits a 50% sharp drop in the load coefficient of blade 2 at the leading edge, i.e., within the range of $0 \leq m \leq 0.2$. As m increases, the reduction gradually slows down and continues up to near $m = 0.8$. In contrast, for Mode 3 relative to the original flow field, the reduction in the load coefficient of blade 2 is only 25%, and the range of reduction is also reduced to $m = 0.6$.

Figure 10b is a comparative graph of the load coefficients for blade 2 at the shroud among mode 1, mode 3, and the original flow field. Compared to the original flow field, mode 1 shows a 20% reduction in the load coefficient across the entire shroud flow surface, whereas mode 3 exhibits a 9% reduction merely within the range of $0.4 \leq m \leq 0.8$, with both range and intensity less than mode 1.

From the analysis above, it can be concluded that blade 2's loading coefficient in mode 3 is higher than in mode 1. According to the blade loading Formula (11), the area enclosed by the loading curve and the x-axis represents the difference in circulation (useful work); hence, mode 3 has a higher circulation difference than mode 1, ultimately resulting in mode 3 exhibiting a higher pump head than mode 1.

In conclusion, the reasons for mode 1's lower head compared to mode 3 are: (1) the reduction of loading at the leading edge of the blades on the hub surface; (2) the overall reduction of blade loading on the shroud surface.

5.2. Blade Pressure

According to Formula (12), the blade loading is essentially the pressure difference between PS and SS. Therefore, this section further analyzes the reason why the head of mode 3 is higher than that of mode 1 from the perspective of blade pressure distribution.

Pressure loading:

$$p_{s,PS} - p_{s,SS} = \frac{2\pi}{Z} \rho \bar{v}_m \frac{\partial(v_u r)}{\partial m} \qquad (12)$$

Figure 11 illustrates the static pressure distribution curves at the hub section of mode 1, mode 2, and the original. Where m denotes the spanwise coefficient, extending from 0 to 1, signifying a direction from outlet to inlet.
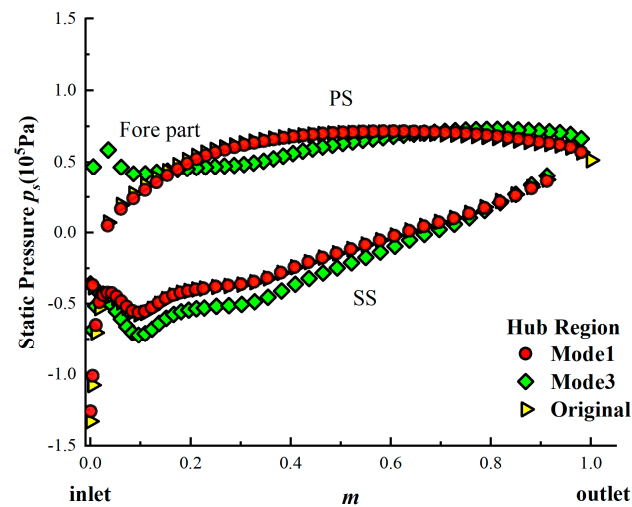
Figure 11. Blade pressure comparison in the hub section at the design point under non-uniform suction flow among mode 1, mode 3, and the original.

In the hub static pressure distribution profile for mode 1, a drop in static pressure is observed at the leading edge ($0 \leq m \leq 0.2$) on the pressure side (PS) of blade 2, while an overall increment is noted on the suction side (SS) compared with mode 3.

Given the correlation between blade loading and pressure differential, as delineated in Formula (12), this dual superimposition effect brings on a pronounced drop in the loading of blade 2 in mode 1, as depicted in Figure 10a. Conversely, the hub static pressure distribution for mode 3 demonstrates a dissimilar variation pattern from mode 1, with a marked distinction in the recovery of static pressure at the leading edge ($0 \leq m \leq 0.2$) on the PS, culminating in a minor reduction in blade 2′s loading. Thus, the unilateral alteration in static pressure on the PS of blade 2 underlies the discrepancy in hub blade loading distribution.

Figure 12 presents the static pressure distribution profiles of blade 2 at the shroud for modes 1, 3, and the original, respectively. Contrasting the static pressure distributions at the hub, the variances in static pressure at the shroud between the two modes predominantly manifest on the SS. In mode 3, the static pressure on blade 2 is significantly lower than that of the original across the full flow span ($0 \leq m \leq 1$). In mode 1, however, there is only a tiny drop compared with the original. As a consequence, the blade loading at the shroud for blade 2 in mode 1 uniformly remains below that in mode 3, as evidenced in Figure 10b.

From the analysis above, it can be concluded that the blade loading of mode 1 is lower than that of mode 3 for the following reasons: (1) the drop of the leading-edge static pressure of the PS at the hub; (2) the overall rise of static pressure of the SS at the shroud.

Cao [34] has contributed valuable perspectives on the causative factors behind these pressure discrepancies between blade 2 and its counterparts, analyzing from the vantage of vortex and streamline distributions. His scrutiny furnishes a meticulous framework for understanding the static pressure differentials noted between blade 2 in modes 1 and 3.
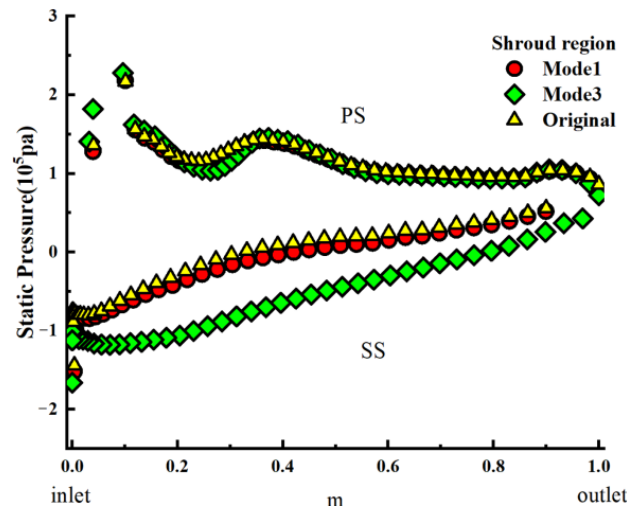
Figure 12. Blade pressure comparison of blade 2 in the shroud section at the design point under non-uniform suction flow among mode 1, mode 3, and the original.

5.3. Streamline and Vortex Structures

To delve into the reasons underlying the static pressure variations observed for blade 2 in Section 5.2, this section presents flow streamlines and vortex distributions at both the hub and shroud of the impeller, as depicted in Figures 13 and 14, respectively.

(**a**)

(**b**)
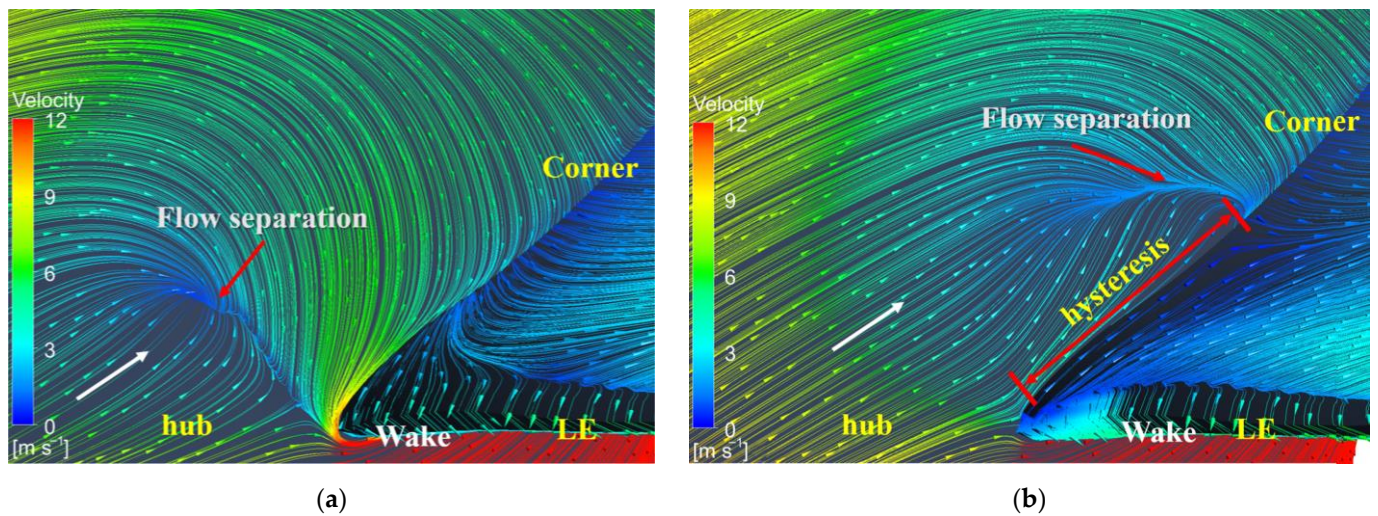
Figure 13. Flow separation at hub region (**a**) mode 1; (**b**) mode 3.

In the result of mode 1, it is evident that four vortex structures are observed, which closely resemble the results obtained from the original flow field. This observation suggests that mode 1 effectively preserves nearly all of the information about the original flow field. However, in mode 3's response, four types of vortex structures are also present but exhibit reduced vortex strength. The underlying reasons for this phenomenon can be analyzed by considering both vortex formation mechanisms and characteristics associated with mode decomposition methods.
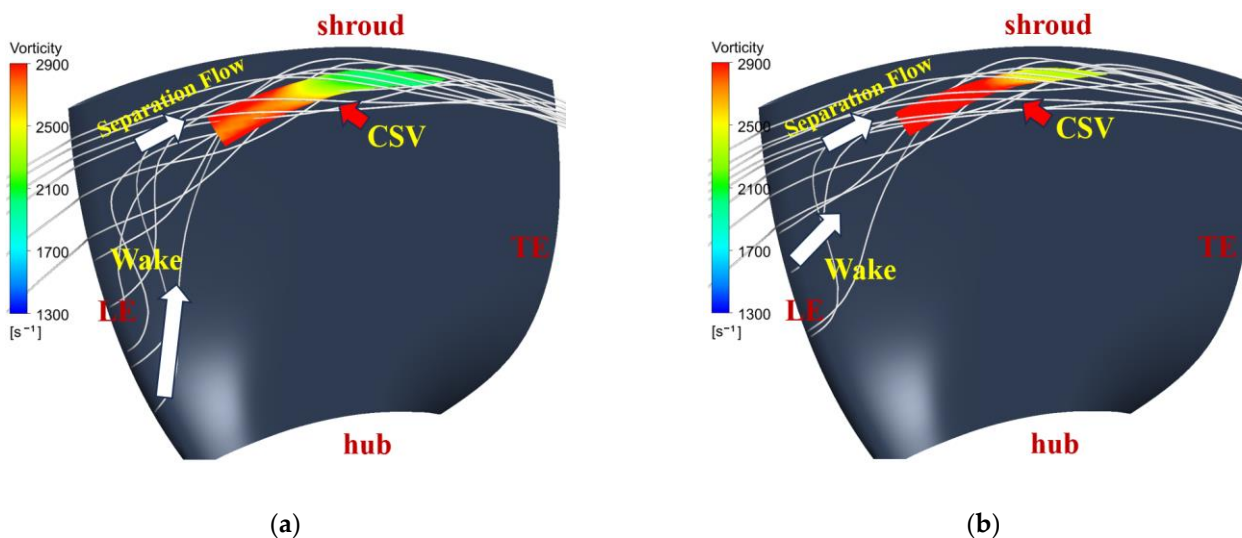
Figure 14. Comparison of 3D streamline at blade 2 shroud region, showing wake evolves into the CSV (**a**) mode 1; (**b**) mode 3.

The interaction between the concentrated vortex (low-energy fluid, Figure 7a) above the inlet flow surface and the impeller induces flow separation due to an adverse pressure gradient at the impeller inlet, resulting in stagnation of the interfering fluid. Furthermore, the rotational motion of the impeller promotes circumferential movement, entraining the surrounding fluid and eventually generating a circumferential vortex (CV), as shown in Figure 9a. The CV significantly influences velocity distribution at the LE, altering the incidence angle and consequently leading to flow separation (Figure 13a).

However, during mode decomposition, as depicted in Figure 7a,d, a certain amount of information related to concentrated vortices is lost for third-order mode with lower energy levels. Hence, the necessary conditions for CV generation are not met, and therefore the position and strength of the separation flow downstream are affected, as shown in Figure 13b. The flow separation observed in mode 3 exhibits a certain degree of hysteresis, occurring at a distance downstream of the leading edge (LE) as it enters the PS of the blade. This flow separation eventually evolves into a wake reversing to the LE, even the SS. Consequently, the fluid at the LE is forced to move downstream at an angle instead of adhering to the PS, resulting in increased static pressure on the PS of blade 2. The hysteresis in flow separation in mode 3 leads to an increase in blade static pressure, thus explaining the observed discrepancy in the static pressure profiles at the LE pressure side between the two modes in Section 5.2, Figure 11.

Following the flow separation, the wake is redirected, bypassing the leading edge and infiltrating the suction side of blade 2. The subsequent redirection of low-energy fluid towards the blade tip, induced by lateral pressure gradients, rapidly interacts with the separated flow along the suction side of the blade. This interaction leads to the entrainment of the surrounding fluid by shed vortex filaments, ultimately evolving into the CSV (Figure 14). The CSV entrains surrounding fluid, causing the streamlines at the shroud of blade 2 to deviate from the suction side and move circumferentially towards the pressure side of an adjacent blade, as illustrated in Figure 15a. In contrast, the hysteretic occurrence of flow separation in mode 3 diminishes the intensity of the wake. Consequently, the wake entering the suction side of blade 2 is reduced, as depicted in Figure 15b. This reduction leads to a decrease in CSV intensity, resulting in streamlines becoming closer to the ideal condition, as depicted in Figure 15b. The reduced curvature radius of the deviated streamlines leads to an increase in centrifugal force, counteracting the original static pressure. This interaction decreases the static pressure on the suction side of blade 2, which explains the observed phenomenon in Figure 12.

(**a**)

(**b**)
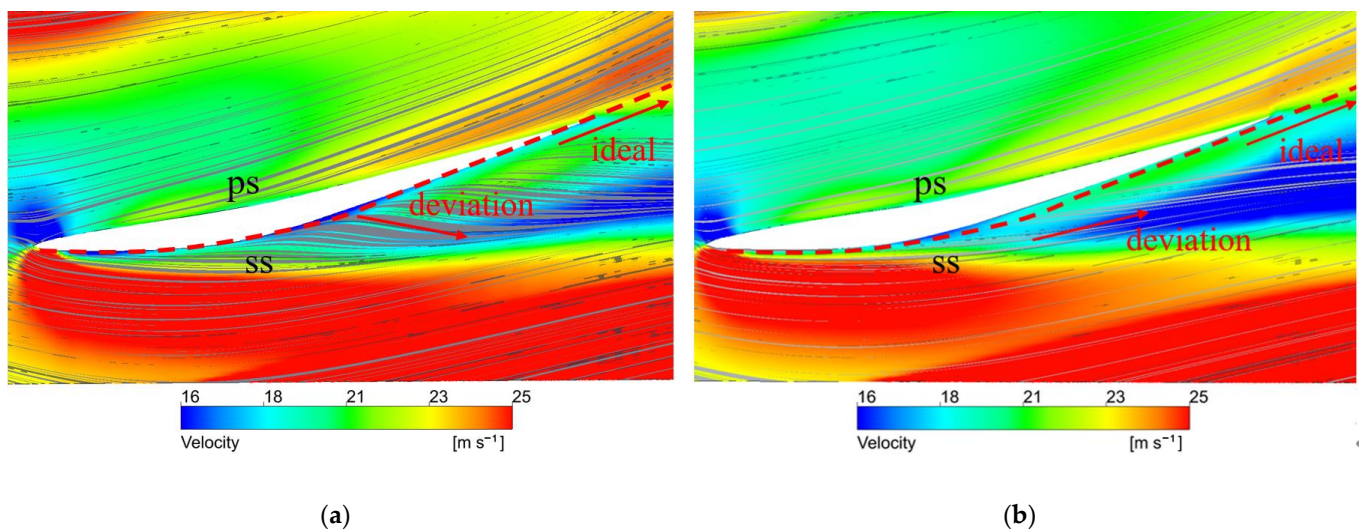
Figure 15. Flow deviation at the tip region of blade 2—(**a**) mode 1; (**b**) mode 3.

Above all, it is revealed that the recovering pump head mainly results from the hysteresis of the flow separation, which is induced by CV.

6. Conclusions

To enhance our understanding of the impact of nonuniform intake flow on waterjet pump performance, we employed the RNG k-ε model and multi-block grids to simulate the dynamics of both individual waterjet pumps and the entire waterjet propulsion system under design conditions. Our study utilized the Proper Orthogonal Decomposition (POD) method to decompose the distorted flow field, allowing for a delicate analysis of the flow structures and their energetic contributions. The key findings from our comprehensive analysis are detailed below, emphasizing the profound implications of our results for optimizing waterjet pump performance:

1. Distinctive energetic contributions and roles of flow modes:

    - The POD (Proper Orthogonal Decomposition) method effectively segmented the velocity flow field within the waterjet propulsion pumps into several modes, each characterized by a unique energy signature organized in descending order. Notably, modes 1 and 2 indicate the formation of the concentrated vortex, while modes 3 and 4 represent its offset in position.

2. Investigations in explaining why, at blade2, mode 3′s head is higher than mode 1:

    - Hub Region: The delayed occurrence of flow separation due to circumferential vortices (CV) resulted in a notable recovery of static pressure at the leading edge on the pressure side (PS). This recovery, coupled with an overall reduction in static pressure on the suction side (SS), leads to increased blade loading at the hub.
    - Shroud Region: The hysteresis in flow separation effectively minimized the reverse flow from the leading edge of the PS into the SS, weakening the intensity of the concentrated separation vortex (CSV), resulting in streamlines becoming closer to the ideal condition, which decreased the static pressure on the suction side. The resultant increased pressure differential between the PS and SS enhanced blade loading.

Ultimately, the lift in blade loading at both the hub and shroud region, results in a higher pump head in mode 3 compared to mode 1.

These conclusions not only advance the theoretical understanding of flow dynamics within waterjet propulsion systems but also provide practical insights that are crucial for the performance enhancement of pump design, e.g., from the perspective of weakening

vortex structure strength that severely influences the blade loading. Besides, by delineating the interactions between various flow structures and pump components, this study fills a significant gap in the application of dimensionality reduction techniques in the analysis of distorted fields within waterjet pumps. We hope that our findings could lead to more efficient and robust waterjet pump systems.

Author Contributions: Conceptualization, R.Y.; methodology, P.C.; software, R.Y. and X.L.; supervision, J.Z. and R.Z.; Writing—original draft, P.C.; writing—review and editing, J.Z. and R.Z.; Funding acquisition, G.W. All authors have read and agreed to the published version of the manuscript.

Data Availability Statement: Relevant data can be found in this article.

Conflicts of Interest: Author Gang Wu was employed by Zhejiang Doyin Technology Co., Ltd. The remaining authors declare that the research was conducted in the absence of any commercial or financial relationships that could be construed as a potential conflict of interest.

Nomenclature

CSV	Concentrated separation vortex
CV	Circumferential vortex
LE	Leading edge
TE	Trailing edge
PS	Pressure side
SS	Suction side
C_L	Normalized blade loading

References

1. Park, W.G.; Jang, J.H.; Chun, H.H.; Kim, M.C. Numerical flow and performance analysis of a water-jet propulsion system. *Ocean Eng.* **2005**, *32*, 1440–1461. [CrossRef]
2. Park, W.G.; Yun, H.S.; Chun, H.H.; Kim, M.C. Numerical flow simulation of flush type intake duct of waterjet. *Ocean Eng.* **2005**, *32*, 2107–2120. [CrossRef]
3. Ni, Y.Y.; Liu, W.M. Research Progress on Pump-Jet Propulsors. *Ship Eng.* **2013**, *42*, 1–5.
4. Zhang, Y.; Wu, P.; Wang, Z. A Review on Hydrodynamic Performance and Design of Pump-Jet: Advances, Challenges and Prospects. *J. Mar. Sci. Eng.* **2020**, *8*, 430.
5. Matsumoto, K.; Tanaka, H.; Ozawa, H. Optimization of Design Parameters of Water Jet Propulsion System. In Proceedings of the FAST93, Yokohama, Japan, 13–16 December 1993.
6. Duerr, P.; Von Ellenrieder, K.D. Scaling and numerical analysis of nonuniform waterjet pump inflows. *IEEE J. Ocean Eng.* **2015**, *40*, 701–709. [CrossRef]
7. Bulten, N.W.H. Numerical Analysis of a Waterjet Propulsion System. Ph.D. Thesis, Eindhoven University of Technology, Eindhoven, The Netherlands, 2006.
8. Van Esch, B.P.M. Performance and radial loading of a mixed-flow pump under non-uniform suction flow. *J. Fluids Eng.* **2009**, *131*, 051101. [CrossRef]
9. Laiping, Z.; Xiaogang, D.; Lei, H.; Ming, L.; Xin, H. The opportunity and grand challenges in computational fluid dynamics by exascale computing. *Acta Aerodyn. Sin.* **2016**, *34*, 405–417.
10. Zhang, H.X. Investigations on fidelity of high order accurate numerical simulation for computational fluid dynamics. *Acta Aerodyn. Sin.* **2016**, *34*, 1–4.
11. Berkooz, G.; Holmes, P.; Lumley, J.L. The Proper Orthogonal Decomposition in the Analysis of Turbulent Flows. *Annu. Rev. Fluid Mech.* **1993**, *25*, 539–575. [CrossRef]
12. Holmes, P.; Lumley, J.L.; Berkooz, G.; Rowley, C.W. *Turbulence, Coherent Structures, Dynamical Systems and Symmetry*, 2nd ed.; Cambridge University Press: New York, NY, USA, 2012.
13. Rowley, C.W.; Dawson, S.T.M. Model Reduction for Flow Analysis and Control. *Fluid Mech.* **2017**, *49*, 387–417. [CrossRef]
14. Taira, K. Proper Orthogonal Decomposition in Fluid Flow Analysis: 1. Introduction. *J. Jpn. Soc. Fluid Mech.* **2011**, *30*, 115–123.
15. Taira, K. Proper Orthogonal Decomposition in Fluid Flow Analysis: 2. Applications. *J. Jpn. Soc. Fluid Mech.* **2011**, *30*, 263–271.

16. Canuto, D.; Taira, K. Two-Dimensional Compressible Viscous Flow Around a Circular Cylinder. *J. Fluid Mech.* **2015**, *785*, 349–371. [CrossRef]
17. Wang, J.H.; Tian, S.L. Proper orthogonal decomposition of flow past parallel twin cylinders. *Phys. Gases* **2023**, *8*, 46–54.
18. Song, W.; Keane, A.J. Surrogate Based Aerodynamic Shape Optimization of a Civil Aircraft Engine Nacelle. *Am. Inst. Aeronaut. Astronaut.* **2007**, *45*, 2565–2574. [CrossRef]
19. Chen, X. *Research on Flow Field Analysis and Performance Optimization in Centrifugal Pumps Based on Eigenvalue Decomposition*; Lanzhou University of Technology: Lanzhou, China, 2022.
20. Ye, C.L.; Huang, W.; Zheng, Y.; Wang, F. Applicability of Modal Decomposition Method to Flow around Hydrofoil. *J. Hydrodyn.* **2023**, *38*, 329–337.
21. Tang, X.; He, W.; Guo, Y.; Peng, R. Time-frequency characteristics of unsteady aerodynamic forces for feathered wind turbine airfoil under tower blade interaction. *Chin. J. Theor. Appl. Mech.* **2023**, *55*, 588–598.
22. Ghoreyshi, M.; Jirásek, A.; Cummings, R.M. Reduced order unsteady aerodynamic modeling for stability and control analysis using computational fluid dynamics. *Prog. Aerosp. Sci.* **2014**, *71*, 167–217. [CrossRef]
23. Dowell, E.H.; Hall, K.C. Modeling of fluid-structure interaction. *Annu. Rev. Fluid Mech.* **2001**, *33*, 445–490. [CrossRef]
24. Brunton, S.L.; Noack, B.R. Closed-loop turbulence control: Progress and challenges. *Appl. Mech. Rev.* **2015**, *67*, 050801. [CrossRef]
25. Svenson, U.; Patel, V.; Li, H. Performance Assessment of the Waterjet Propulsion System through a Combined Analytical and Numerical Approach. *Fluids* **2016**, *4*, 158.
26. Hu, Z.; Chen, D.; Liu, Y.; Zhang, X. Numerical Analysis on Self-Propulsion of a Waterjet-Propelled Ship with Different Propulsion Models. *Appl. Sci.* **2020**, *10*, 6354.
27. Li, W.; Noblesse, F. Numerical Simulation and Uncertainty Analysis of an Axial-Flow Waterjet Pump. *J. Mar. Sci. Eng.* **2018**, *6*, 2.
28. Chang, S.P.; Wang, Y.S. Prediction of waterjet performance using k-ε turbulence model. *J. Huazhong Univ. Sci. Technol.* **2012**, *40*, 88–95.
29. Liu, H.; Wang, Z.; Liu, D. Comparison of Cavitation in Two Axial-Flow Water Jet Propulsion Pumps. *Processes* **2023**, *11*, 2137.
30. Pei, J.; Zhou, L.; Yuan, S. Research on Cavitation Wake Vortex Structures Near the Impeller Tip of a Water-Jet Pump. *Energies* **2019**, *12*, 2154.
31. Cao, P.Y.; Wang, Y.; Qian, K.X.; Li, G.D. Comparisons of hydraulic performance in permanent maglev pump for water-jet propulsion. *Adv. Mech.* **2014**, *10*, 438176. [CrossRef]
32. Bonaiuti, D.; Zangeneh, M. On the coupling of inverse design and optimization techniques for the multiobjective, multipoint design of turbomachinery blades. *J. Turbomach.* **2009**, *131*, 021014. [CrossRef]
33. Bonaiuti, D.; Zangeneh, M.; Aartojarvi, R.; Eriksson, J. Parametric design of a waterjet pump by means of inverse design, CFD calculations and experimental analyses. *J. Fluids Eng.* **2010**, *132*, 031104. [CrossRef]
34. Cao, P.Y.; Wang, Y.; Kang, C.; Li, G.D.; Zhang, X. Investigation of the role of non-uniform suction flow in the performance of water-jet pump. *Ocean Eng.* **2014**, *140*, 258–269. [CrossRef]